Analyst

PAPER

View Article Online
View Journal | View Issue

Cite this: *Analyst*, 2015, **140**, 5324

Incorporation of a FRET dye pair into mesoporous materials: a comparison of fluorescence spectra, FRET activity and dye accessibility

Susanne Widmer,[a,b] Michael J. Reber,[c] Patrick Müller,[c] Catherine E. Housecroft,[b] Edwin C. Constable,[b] René M. Rossi,[a] Dominik Brühwiler,[c] Lukas J. Scherer[a] and Luciano F. Boesel*[a]

Received 29th April 2015,
Accepted 9th June 2015

DOI: 10.1039/c5an00850f

www.rsc.org/analyst

Fluorescein and rhodamine B modified mesoporous silica particles were synthesized by post-grafting and co-condensation approaches. The materials exhibited different pore size distributions, particle shapes and sizes. The materials were characterized by nitrogen sorption, scanning electron microscopy and fluorescence spectroscopy. The Förster resonance energy transfer between the selected dye pair was explored for the different materials by exposure to various concentrations of gaseous ammonia. A logarithmic increase in rhodamine B emission with increasing ammonia concentration was observed for both post-grafted and co-condensed materials. The dye accessibility by ammonia gas in the silica framework of mesoporous materials was evaluated by using a flow cell gas sensor setup built in-house. Response to ammonia gas and recovery with nitrogen gas are explained by comparing the structure properties and dye loading of the materials. The post-grafted dye modified silica showed better performance in terms of reversibility and recovery.

1 Introduction

Mesoporous silica can be functionalized with organic functional groups, allowing this versatile material to be used in many applications, in particular the separation and adsorption of gaseous species. Recently, the potential of mesoporous silica in the field of luminescence sensing has been demonstrated.[1–13]

Mesoporous silicates can be prepared by direct co-condensation, but grafting procedures are a convenient method for their functionalization. Postsynthetic functionalization is favored over co-condensation if the groups to be integrated are not sufficiently stable under the harsh conditions of mesoporous silica synthesis, or if more regular silicates with a narrower pore size distribution (PSD) are desired.[14] One drawback of grafting is that the entire surface may not be accessible, which then leads to an inhomogeneous distribution with more grafted groups on the external surface and near the pore entrances.[14–17] The solvent in which the postsynthetic functionalization is performed, as well as the type of organosilane used contribute to the final functional group distribution on the mesoporous material.[17–19] A preferential coupling to the pore openings during the initial stage of the grafting procedure prevents the diffusion of further organosilanes into the center of the pores and can lead to a lower degree of functionalization.[14,18] In contrast, co-condensation does not have the issue of inhomogeneous functional group distribution. Since organic groups are introduced during the synthesis of the material they tend to be distributed evenly throughout the entire framework. Moreover, pore blocking is not a problem, since the organic functionalities are integral components of the silica matrix.[14] However, the organic moiety to be incorporated must withstand the synthesis conditions and high concentrations of these organic groups can have negative effects on the formation of the material (mesoscopic order, PSD, particle shape and size).[14–16,20–22] One study concluded that the accessibility of co-condensed functionalized SBA-15 (Santa Barbara Amorphous 15) is diminished compared to postgrafted SBA-15.[23] However, by subsequent coupling of the functional groups with organic residues, desired properties such as luminescence and sensing can be achieved for both materials.

Here we report the synthesis of fluorescein and rhodamine dye-modified mesoporous silica using postsynthetic and co-

[a]*Empa, Swiss Federal Laboratories for Material Science and Technology, Laboratory for Protection and Physiology, Lerchenfeldstr. 5, 9014 St. Gallen, Switzerland. E-mail: luciano.boesel@empa.ch; Fax: +41 58 765 7499; Tel: +41 58 765 7393*
[b]*Department of Chemistry, University of Basel, Spitalstrasse 51, 4056 Basel, Switzerland*
[c]*Institute of Chemistry and Biological Chemistry, Zurich University of Applied Sciences (ZHAW), Einsiedlerstrasse 31, 8820 Wädenswil, Switzerland*

condensation methods. Fluorescein and rhodamine constitute an established dye pair that exhibits Förster resonance energy transfer (FRET), a phenomenon that describes the non-radiative transfer of energy between two chromophores under appropriate conditions.[24] Additionally, the influence on the FRET activity was investigated for each material by immobilizing in a xerogel film and recording fluorescence spectra in the absence and presence of gaseous ammonia. Since the fluorescence quantum yield of fluorescein is increased at higher pH, the overlap between fluorescein emission and rhodamine absorption is enhanced in the presence of ammonia. The accessibility of the dyes to NH_3 is discussed on the basis of gas sensor measurements in a gas flow cell optical sensor setup.

2 Experimental details

2.1 Synthesis of fluorescein/rhodamine modified SBA-15 particles

Synthesis of SBA-15 particles (SBAs). Spherical SBAs were synthesized according to the literature[18,25,26] by adding a solution of hexadecyltrimethylammonium bromide (0.465 g; Fluka) in deionized H_2O (20 mL) to a solution of Pluronic P123 (3.10 g; $EO_{20}PO_{70}EO_{20}$, M_{av} = 5800, Aldrich) in 1.5 M aqueous HCl (50 mL; Aldrich). After the addition of ethanol (7.8 mL; Aldrich), the mixture was stirred vigorously and tetraethoxysilane (10 mL; TEOS, Fluka) was added dropwise. After stirring for 2 h at room temperature (RT), the mixture was transferred to a Teflon-lined autoclave and kept at 78 °C for 72 h. The product was collected by filtration, washed with deionized H_2O (50 mL), and dried at RT. Calcination was performed at 500 °C for 16 h with a heating rate of 1.2 °C min^{-1}.

Functionalization with 3-aminopropyltriethoxysilane (APTES). Amino-functionalization of SBA was carried out following a method similar to that reported in literature.[18] The mesoporous silica (400 mg) was dispersed in dry toluene (20 mL; AcrosOrganics, 99.85%, <0.003% H_2O) and APTES (40 μmol; Aldrich) was added under N_2. For smaller batches 100 mg of SBA was dispersed in 5 mL of dry toluene and APTES (10, 20 or 40 μmol respectively) was added under N_2. After vigorous stirring under N_2 for 10 min, the dispersion was transferred to centrifuge tubes and centrifuged at 7000 rpm for 5 min. The supernatant liquid was decanted and the residual pellet was re-dispersed in toluene and centrifuged 3 times. The amino-functionalized silicas, SBA-NH_2 1–4, were cured at 70 °C for 16 h. SBA-NH_2 1 corresponds to the amino-functionalized SBA obtained from the larger batch. SBA-NH_2 2–4 correspond to the 100 mg batches functionalized with 10 (SBA-NH_2 2), 20 (SBA-NH_2 3) or 40 μmol (SBA-NH_2 4) APTES respectively.

Labeling with fluorescein/rhodamine (F/R) by the post-grafting (PG) method. Fluorescein 5-isothiocyanate (FITC isomer I, Aldrich) and rhodamine B isothiocyanate (RBITC, Aldrich) were coupled to amino-functionalized mesoporous silica (SBA-NH_2 1–4) following a literature[18] method by dispersing amino-functionalized silica (100 mg) in dry ethanol (5 mL; AcrosOrganics, 99.5%, <0.005% H_2O) under N_2. An equal amount of ethanol was used to dissolve the corresponding dyes (total 10, 20 or 40 μmol respectively, for dye pairs half amount of each). The dye solution was added to the silica dispersion. After stirring for 5 h at RT under N_2, the dispersion was transferred to centrifuge tubes and centrifuged at 7000 rpm for 7 min. The supernatant liquid was decanted and the pellet re-dispersed in ethanol and centrifuged 10 times. The dye modified mesoporous silica, PG SBA FR 1–4 and PG SBA F/R 1, was dried at 70 °C for 1 h. The numbers correspond to the initial SBA-NH_2 were also used for the dye labeling products.

Synthesis of fluorescein/rhodamine modified SBA by co-condensation. Co-condensed fluorescein and rhodamine modified SBA-15 particles were synthesized using procedures from ref. 25, 27 and 28 with minor optimization. Fluorescein isothiocyanate (FITC isomer I, Aldrich) and rhodamine B isothiocyanate (RBITC, Aldrich) were coupled to APTES by dissolving the dyes separately in ethanol (Aldrich). After addition of APTES to each dye solution, the mixture was stirred in the dark for 24 h. The amounts used for the coupling of APTES with the dye are shown in Table 1.

P123 and KCl (Fluka) were dissolved in deionized H_2O and HCl (32%; Aldrich). Then 1,3,5-trimethylbenzene (TMB; Aldrich) was added. After stirring for 2 h in ethanol, TEOS (Fluka) and the corresponding amount of APTES-dye in ethanol were added. The amounts of the different reaction components used for the syntheses are given in Table 2. The mixtures were stirred for 30 min before being transferred to a Teflon-lined autoclave and kept at 60 °C for 4 h. The products were collected by filtration, washed with deionized H_2O (50 mL), and dried at 120 °C for 20 min. The structure directing agent was removed by Soxhlet extraction in ethanol and co-condensed mesoporous materials, CoCo SBA FR HD/LD, were obtained.

2.2 Thin film preparation

General sol preparation. The sol preparation was performed according to ref. 29. FITC/RBITC sols were prepared by dissol-

Table 1 Dye–APTES solutions prepared for the synthesis[a]

Sample	FITC/RBITC [μmol]	APTES [mL]	EtOH [mL]
CoCo SBA FR HD	19/20	0.01	1
CoCo SBA FR LD	19/20	1	10

[a] Sample denomination: CoCo: co-condensed; SBA: mesoporous material; F: fluorescein; R: rhodamine; HD: high dye loading; LD: low dye loading.

Table 2 Synthesis conditions for the synthesis of FITC/RBITC labeled co-condensed SBA

Sample	P123 [g]	KCl [g]	H_2O [mL]	HCl [g]	TMB [g]	TEOS [mL]	APTES-dye [μL]
CoCo SBA FR HD	0.5	0.76	15	3.0	0.38	1.1	150
CoCo SBA FR LD	1.0	1.5	30	5.9	0.76	2.3	250

ving the desired amount (2.5, 10, 20 μmol) of the dye in 5 mL of ethanol (Fluka). After sonication (UltrasonicCleaner from VWR, 45 kHz, 80 W) of the solution for 10 min at RT, methyltriethoxysilane (1.793 mL; Aldrich) and 3,3,3-trifluoropropyltrimethoxysilane (0.576 mL; Aldrich) were added. After a further 10 min of sonication, 0.1 M HCl (0.08 mL; Aldrich) and deionized H_2O (80 μL) was added to the solution. The sol was sonicated for another 20 min and aged for 24 h at RT. Sols without dyes (unlabeled) used for the immobilization of the particles were prepared the same way.

Xerogel film preparation for fluorescence measurements. 5 μL of the sol solution was solvent cast on PMMA substrates (4.5 × 4.5 × 0.5 mm^3; foil from microfluidic ChipShop) and dried in an oven at 70 °C for 12 days. Particles were immobilized in the xerogel coating by dispersing 1 mg of the corresponding SBA material in 80 μL of aged unlabeled sol solution. The solvent-casting procedure was the same for these sols as for sols without particles. Particle coatings were dried at 70 °C for 2 days.

Xerogel film preparation for gas sensor measurements. 20 μL of aged sol were solvent cast on cut PMMA substrates (1.5 × 1.5 × 0.1 cm^3; microscope slides from microfluidic ChipShop) and dried in an oven at 70 °C for 12 days. Particles were immobilized in the xerogel coating by dispersing 1.5 mg of the corresponding SBA material in 50 μL of aged unlabeled sol solution. The solvent-casting procedure was the same for these sols as for sols without particles. Particle coatings were dried at 70 °C for 2 days.

2.3 Characterization methods

Fluorescence measurements. Fluorescence measurements were performed according to ref. 29. Fluorescence spectra were recorded in the range of 495–700 nm on a Biorad Fluorescence spectrophotometer. The small xerogel-coated PMMA plates were horizontally pinched into the wells of a microtitre well-plate at the same height. The plates were exposed to NH_3 gas by adding 20 μL of the desired aqueous NH_3 solutions to the well bottom by microsyringe. The well plate was then covered by a lid and wrapped with Parafilm. Before each fluorescence measurement, the loaded well plate was stored in a conditioned room (21 °C, 50% rel. air humidity) for 30 min to ensure the same measurement conditions. The NH_3 vapour concentrations within the wells were calculated based on the partial pressure of NH_3.[30,31] To compensate possible humidity response, the coatings were exposed three times to H_2O vapour by adding 20 μL of H_2O to the well bottom by microsyringe. The average of the observed intensities was taken as the reference intensity for the NH_3 experiments.

Determination of dye content in SBAs. The amount of coupled FITC and RBITC was determined by dissolving the sample (usually 1–4 mg) in 0.2 M aqueous NaOH and measuring the UV-visible spectra of the resulting clear solution on a Biotek spectrophotometer. The molar extinction coefficients for FITC (ε = 76 000 M^{-1} cm^{-1}) and RBITC (ε = 37 700 M^{-1} cm^{-1}) in 0.2 M NaOH were obtained with a standard deviation of 6% from four stock solutions prepared as follows: (1) FITC and RBITC were stirred separately in 0.2 M NaOH until complete dissolution. (2) FITC and RBITC were combined in a molar ratio of 1 : 1 in 0.2 M NaOH and stirred until complete dissolution. (3) FITC and RBITC were stirred separately in ethanol until complete dissolution. A corresponding amount of APTES was added and the reaction mixture was stirred for 16 h. After evaporation of the solvent, the residue was dissolved in 0.2 M NaOH. (4) FITC and RBITC were combined in a molar ratio of 1 : 1 in ethanol until complete dissolution. Subsequent treatment was as with (3). The addition of mesoporous silica to the dilution series showed no significant effect on the extinction coefficient.

Scanning electron microscopy (SEM). Cuts were obtained by solvent casting the sols on a silicon wafer and drying for 12 days. The wafer was broken in the middle over a sharp edge. The samples were Au/Pd sputtered with a device from Leica. The images were recorded on a Hitachi S4000 instrument.

Confocal laser scanning microscopy (CLSM). CLSM images were taken with an Olympus BX 60 microscope equipped with a FluoView detector. Optical slices of the center of the particles were obtained by exciting with lasers operating at 488 and 543.5 nm.

Optical microscopy. The images were recorded on the coatings prepared for the gas sensor measurements using an optical microscope from Keyence.

Nitrogen sorption measurements. Nitrogen adsorption isotherms were measured at −196 °C using a NOVA 3000e Surface Area and Pore Size Analyzer (Quantachrome). Prior to measurement, the samples were vacuum degassed at 80 °C for 3 h. Pore size distributions (d_{NLDFT}) and total surface area (S_{BET}) were calculated from the NLDFT[32] and the BET[33] methods. External surface area (S_{ext}) was determined by the α_s method.[34] Total pore volume (V_{tot}) was calculated at a relative pressure of 0.95. The adsorption isotherm was used for all calculations.

Gaussian evaluation. The Gaussian evaluations were performed with the Origin software version 9.

2.4 Gas sensor measurements

Procedure. The gas sensor measurements were performed with an in-house built flow cell gas sensor.[29] The setup is illustrated in Fig. 1. The xerogel-coated plates were placed in a flow cell as shown in Fig. 2. The plates were illuminated from the top by a 0.7 W LED of peak wavelength 470 nm (FWHM band-

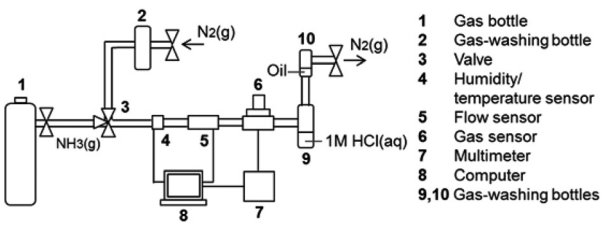

Fig. 1 Flow cell gas sensor setup.[29]

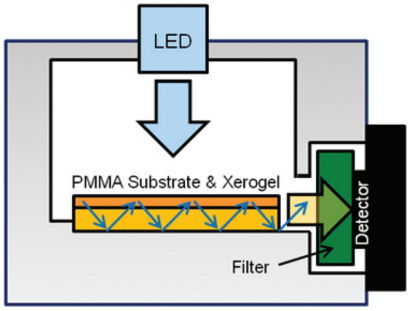

Fig. 2 Schematic of the gas sensor box, where the coated PMMA substrate is deposited.

width 25 nm) purchased from Thorlabs. To measure fluorescence emission, the photodetector was placed orthogonal to the incoming radiation, therefore the PMMA sample plate acted as a waveguide of the emitted light to the detector. Additionally, an optical longpass filter was placed in front of the detector, which only allowed passage of light above 550 nm (FEL0550; Thorlabs). The inside of the flow cell was painted black to reduce reflections of the direct light. Electronic readout was based on a phototransistor circuit and a LabView-controlled digital multimeter. The flow cell was connected to gas supplies as depicted in Fig. 1. The gas flow could be switched between NH_3/N_2 mixture and N_2 using manual valves. During the experiments, the flow rate (800 mL ± 50 mL min^{-1}), the temperature (20 ± 2 °C), and the humidity (<4%) were monitored in the line using a CMOSens EM1 (Sensirion) and an MSR 145 (Sensirion) respectively. Custom mixed gases 49.7 ppm ± 2% rel. NH_3, 99.6 ppm ± 2% rel. NH_3, 504.9 ppm ± 2% rel. NH_3, 0.101 ± 1% rel. NH_3 in N_2 (≥99.8%) and pure N_2 gas were acquired from Carbogas.

Measurement and evaluation. Before each measurement, the system was flushed with N_2 gas for 5 min. An experiment always started with a 300–600 s N_2 gas flush followed by a flush with an NH_3 gas mixture. Raw data from the one cycle measurements were plotted in Microsoft Excel and illustrated without further processing. The thermal drift of the cycle measurement of PG SBA FR 1 was corrected by fitting a double polynomial equation to the turning point of each cycle (valley, lowest point of N_2 recovery). The signal noise was reduced by using a fifth order Butterworth low-pass filter with 5 mHz cut-off frequency.

3 Results and discussion

3.1 Comparison of structure properties

The morphology of the SBAs was examined using SEM (Fig. 3). Purely siliceous SBA particles were spherical (Fig. 3c) with a diameter in the range of 4–12 μm. The relatively narrow PSD is typical for SBA that has a small tail extending in to the microporous range (Fig. 4).[35] The average pore size was 6 nm (Table 3). Labeling did not influence the morphology of the SBA (Fig. 3d). The CoCo SBA FR LD, synthesized with low APTES-dye concentrations, produced well-shaped spherical particles with similar diameters between 2 and 4 μm (Fig. 3b). However, CoCo SBA FR LD showed a broad PSD with a width at half maximum of about 9 nm and a pore size of about 10 nm (Fig. 4). The increase and broadening in pore size results from the increased concentration of organics in the mother liquid.

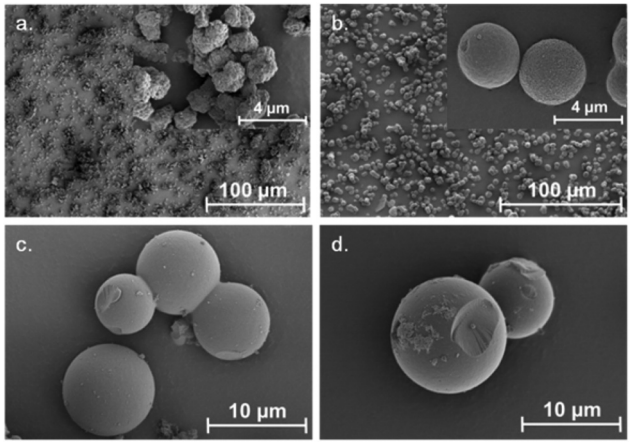

Fig. 3 SEM illustrations of synthesized particles: (a) CoCo SBA FR HD, (b) CoCo SBA FR LD, (c) SBA, (d) PG SBA FR 1.

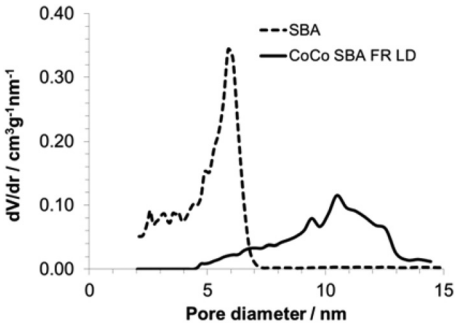

Fig. 4 Pore size distribution of unmodified SBA and CoCo SBA FR LD.

Table 3 Properties of investigated SBA materials

Sample	d_{NLDFT}[a] [nm]	S_{BET} [m^2 g^{-1}]	V_{tot} [cm^3 g^{-1}]
CoCo SBA FR HD	7	228	0.39
CoCo SBA FR LD	10	215	0.47
SBA-15	6	801	0.79
SBA-NH_2 1	6	755	0.79
SBA-NH_2 2	6	587	0.70
SBA-NH_2 3	6	505	0.61
SBA-NH_2 4	6	436	0.56
PG SBA FR 1	6	753	0.77
PG SBA FR 2	6	515	0.59
PG SBA FR 3	6	329	0.42
PG SBA FR 4	6	292	0.35

[a] Average pore diameter of the mesopores.

These organic molecules dissolve in the organic phase inside of the structure-directing agent leading to an expansion of the micelles. CoCo SBA FR HD particles were irregular (Fig. 3a). The PSD is also very broad and undefined, indicative of a poor long range ordering of the material. High concentrations of organics in the synthesis mixture, in this case TMB and higher amount APTES-dye, have a large effect on the particle morphology and PSD.[36] The initial material for all post-grafted materials was SBA with a pore size of around 6 nm (Table 3). The amount of grafted organic moieties increased from samples SBA-NH_2 1–4 to PG SBA FR 1–4, but the pore sizes showed negligible changes, since the introduced amount of dye is in the nanomolar range per mg of silica and the distribution of the grafted APTES molecules is non-uniform.[14,37] The extent of organic modification is possibly too low for an unambiguous effect on the pore size, but sufficient enough to affect the pore volumes and BET surface areas, which show a decreasing trend with increasing amount of grafted molecules (Table 3).

3.2 Comparison in dye content

Table 4 lists the amounts of dyes detected on the different SBA samples. The resulting dye ratios were similar in both CoCo materials, as well as in the PG materials, indicating same coupling behavior. In all cases, FITC is more likely to be integrated into the material than RBITC. A possible explanation of this is the larger steric hindrance of RBITC due to its two additional ethyl groups on each site of the xanthene structure making the entry into the pores more difficult, especially if the pores are partially blocked by already coupled dyes. Furthermore, rhodamine B dyes are reported to preferentially form dimers and trimers in concentrated ethanol solutions[38] leading to an impeded diffusion of the dye aggregates into the mesopores and probably also to aggravated coupling to the amino groups because of the restricted dye mobility. A higher dye aggregation tendency can be expected in the reaction mixture for the dye labeling of PG SBA R 1, because of the high dye concentration and the fact that there is no other type of dye molecules disturbing the aggregation process. This can be the reason for the comparably lower RBITC coupling yield for PG SBA R 1. Another reason for the reduced RBITC coupling may be the ability to form hydrogen bonds with the hydroxyl-groups of the silica surface. By forming hydrogen bonds with the silica surface, FITC is relatively fixed, promoting the reaction with surface bound amino groups. The given yields of coupled dyes for CoCo SBAs are related to the initial dye amount introduced into the synthesis (Table 2). The yields for PG SBAs correspond to the dye amount coupled assuming a 100% yield in post-synthetic amino-functionalization. For fluorescein and rhodamine modified PG SBAs, the coupling to 50% of the amino groups was considered as 100% yield for each dye. With exception of the FITC yield of CoCo SBA FR HD, all yields were found to be below 20%. The low coupling yield for the CoCo material can be explained by only a fraction of APTES coupled to the dyes, resulting in less dye incorporation during the synthesis and some dye being washed out or degraded during Soxhlet extraction to remove the template.

Comparing CoCo SBA FR HD and CoCo SBA FR LD, the dye concentration was higher in CoCo SBA FR HD which leads to a higher amount of FITC-APTES and RBITC-APTES during the SBA synthesis. Furthermore, the APTES concentration was higher in the CoCo SBA FR LD synthesis which influences the co-condensation, since more free APTES is available. The free APTES possibly competes with APTES dye during incorporation into the silica network, leading to the observed lower coupling yield in CoCo SBA FR LD.

The postsynthetic amino-functionalization was most likely <100% leading to underestimated coupling yields for the PG materials. Furthermore, pore blocking from already coupled dyes or the presence of micropores can reduce the accessibility of the amino groups.[39] More material was needed to synthesize the PG SBA F/R and PG SBA FR 1 samples, therefore SBA-NH_2 1 was made in a large batch to ensure that enough material was present for multiple reactions. In a larger batch the grafting procedure tended to produce less amino-functionalized SBAs as can be concluded by comparing PG SBA F/R 1, PG SBA FR 1 and PG SBA FR 2. For equal batches the amount of dye labeling could be measurably tuned by varying the amount of APTES during the synthesis as seen for the samples PG SBA FR 2–4 (Table 4). Hence, the amount of dyes on the mesoporous silica can be tuned by increasing the APTES-dye concentration in the synthesis or by enhancing the postsynthetic amino-functionalization. CLSM measurements show homogenous distributions for FITC as well as RBITC dyes in all SBAs (Fig. 5).

Table 4 Amount of dye calculated per mg silica[a]

Sample	FITC [nmol mg^{-1}]	RBITC [nmol mg^{-1}]	Ratio FITC/ RBITC	Yield FITC [%]	Yield RBITC [%]
CoCo SBA FR HD	5.9 ± 0.4	2.2 ± 0.1	1 : 0.4	46	16
CoCo SBA FR LD	0.35 ± 0.03	0.17 ± 0.01	1 : 0.5	16	9
PG SBA F 1	4.6 ± 0.3			5	
PG SBA R 1		0.35 ± 0.02			0.4
PG SBA FR 1	2.6 ± 0.2	1.9 ± 0.1	1 : 0.7	5	4
PG SBA FR 2	8.0 ± 0.5	5.0 ± 0.3	1 : 0.7	16	11
PG SBA FR 3	16 ± 1	9.1 ± 0.6	1 : 0.6	16	10
PG SBA FR 4	28 ± 2	18 ± 2	1 : 0.6	14	8

[a] Values are given with 6% deviation (ε_{FITC}: 76 000 L mol^{-1} cm^{-1}, ε_{RBITC}: 37 700 L mol^{-1} cm^{-1}). The coupling yields are related to the initial dye amounts introduced during synthesis.

3.3 FRET mechanism explained on the basis of NH_3 response

Spectral investigation. Fluorescein derivatives have been used as sensing species displaying linear dependency over wide ranges of ammonia concentrations.[40–42] FRET-based optical chemosensors for the detection of ammonia have been reported[43–46] and the advantages have been highlighted as they can generate dual or multiple emissions under a single wavelength excitation, resulting in more effective ratiometric

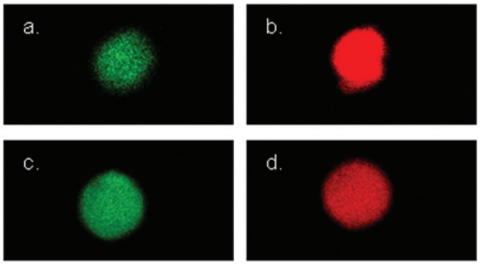

Fig. 5 CLSM illustrations of dye modified SBAs. Top: CoCo SBA FR HD, particle size ~3 μm. Bottom: PG SBA FR 1, particle size ~5 μm. Left: sample was illuminated at 488 nm. Right: illumination at 544 nm.

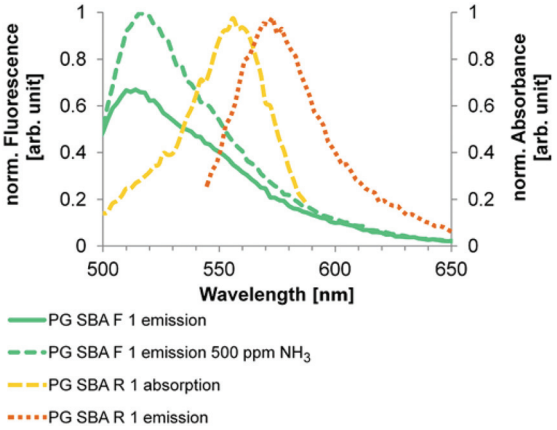

Fig. 6 Emission and absorption spectra of investigated FRET dye pair on SBA particles immobilized in the unlabeled xerogel. The spectral overlap is increasing with increasing formation of fluorescein dianion. Excitation wavelengths: 484 nm (F) and 535 nm (R). The emission of rhodamine B (573 nm) is red-shifted when present in a FRET-system to 595 nm (see Fig. 7).

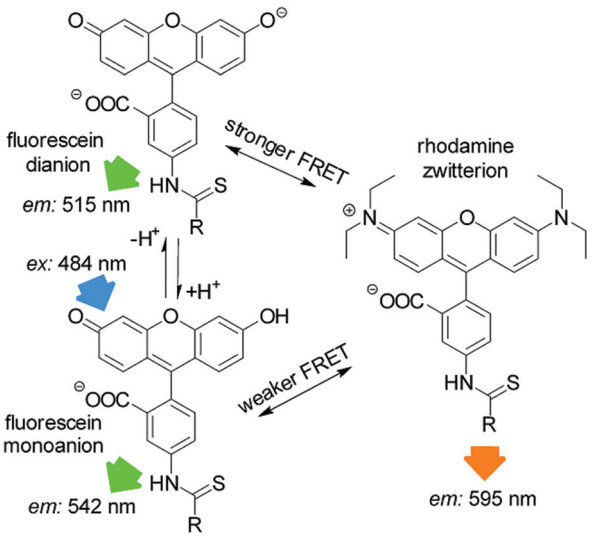

Fig. 7 FRET mechanism between fluorescein and rhodamine. R = coupling to amino-functionalized silica.

detection in comparison to those that need two separate excitation wavelengths.[47] Furthermore, their design can easily be modified by varying the FRET components.

Depending on the ambient pH value, fluorescein exists in cationic, neutral, monoanionic or dianionic forms or as a mixture thereof.[48] Absorption as well as emission spectra are dependent on the presence of species in different protonation states.[48] The acid dissociation constants in solution reported for fluorescein are in the range of $pK_{cationic}$ = 2.00–2.25, $pK_{neutral}$ = 4.23–4.4 and $pK_{monoanionic}$ = 6.31–6.7, depending on the specific conditions and measurement techniques.[48–50] Rhodamine B can be present in a few different species under extreme conditions[51] but only the cationic and zwitterionic forms are fluorescent. The pK_a of the cationic form in solution is in the range of 3.22–4.2, depending on the specific conditions and measurement techniques.[51–54] For spectral investigation of the SBAs, the particles were immobilized in a transparent organic modified xerogel film the properties of which have already been reported.[29] The emission spectrum of PG SBA F 1 shows an emission band at 515 nm and a shoulder at 542 nm, indicating the presence of at least two emittive species, which are assigned to the monoanionic and dianionic forms respectively (Fig. 6). Exposure to NH_3 leads to deprotonation of the monoanionic species forming more dianionic species, which results in an enhancement of its fluorescence. The higher intensity of emission scales to an increase of the quantum yield (Φ = 0.93) and the high molar absorptivity of the dianionic fluorescein form.[48] The absorption spectrum of rhodamine has a peak at 553 nm and a shoulder around 535 nm, which suggests the presence of both fluorescent rhodamine species (Fig. 6). The increase in fluorescein emission upon ammonia exposure leads to a larger overlap of fluorescein emission and rhodamine absorption that results in enhanced FRET efficiency and thus increased rhodamine emission (Fig. 7 and 8).

The wavelength range of the emission bands is comparable for CoCo SBA FR HD and PG SBA FR 1 coatings (Fig. 8a and c). Although, the PG material was found to have less dye content, the fluorescein emission intensity is similar to the CoCo material and rhodamine emission intensity even higher. This observation leads to the conclusion that the high dye loading in the co-condensed material leads to fluorescence quenching. The more intense rhodamine emission in the PG material is based on the determined fluorescein/rhodamine proportion in the materials, being higher for the PG material. CoCo SBA FR LD coatings exhibit comparable low rhodamine emission intensity due to less dye incorporation and the emission band is more blue shifted in comparison to the SBA with higher dye loadings (Fig. 8b). Fig. 8d shows the emission spectra of a FITC and RBITC modified xerogel film. The fluorescence intensity (arb. unit) scale cannot be compared with a, b and c. Detector adjustments were carried out since the measurement under the identical set-up conditions resulted in an overflow of fluorescence intensity. Fig. 9 illustrates the spectral response to NH_3 by the increase of rhodamine maximum fluo-

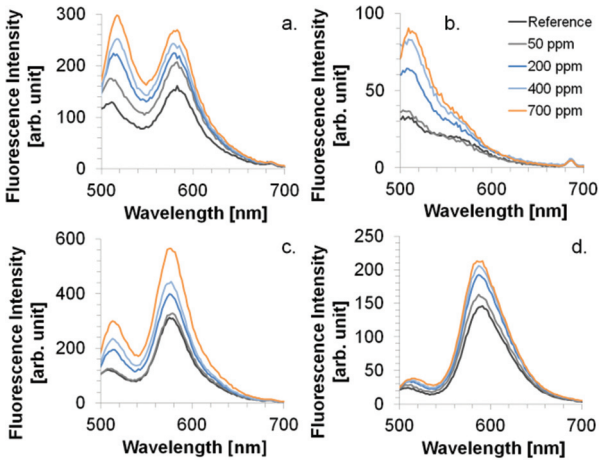

Fig. 8 Spectral behavior upon NH_3 exposure. Coatings: (a) CoCo SBA FR HD, (b) CoCo SBA FR LD, (c) PG SBA FR 1, (d) FITC/RBITC (ratio 4 : 1) modified xerogel film. Excitation wavelength was 484 nm.

rescence emission at *ca.* 580 nm which was similar for the CoCo SBA FR HD and PG SBA FR 1 coatings. The exposure to 1000 ppm of gaseous NH_3 led to a *ca.* 1.5-fold increase of the rhodamine fluorescence intensity. PG SBA FR 2–4 did not respond to NH_3 with an increase of rhodamine fluorescence emission. This observation indicates that higher dye amounts are not necessarily beneficial for this FRET system. A closer look at the fluorescence spectra of the PG SBA FR 3 coating reveals that the fluorescein emission intensity decreased and the rhodamine fluorescence emission intensity remained unchanged although the total dye amount was 5 times higher in comparison to PG SBA FR 1. The larger dye amount probably led on one hand to an enhanced FRET activity because of the higher amount of dye pairs but on the other hand to more fluorescence quenching due to the high dye density on the particles as observed for the co-condensed material. The CoCo SBA FR LD coating shows a better response towards ammonia for concentrations above 400 ppm. However, the rhodamine emission is low in comparison to the more intense fluorescein emission and in addition is close to the fluorescein emission band. Therefore, the increasing intensity of the fluorescein fluorescence emission tail may contribute to the increase of rhodamine fluorescence emission intensity and lead to overestimation of the ammonia response. The contribution of fluorescein fluorescence emission in PG SBA FR 1 was evaluated by fitting Gaussians and is discussed later in this section. The response of the xerogel films with dye ratios of 1 : 1, 4 : 1 and 8 : 1 was similar and also comparable to the particle coatings within standard deviations. This data shows that a higher ratio of donor/acceptor did not lead to a higher FRET efficiency, so that the relative response was independent of the ratio. Since higher amount of dyes can be integrated into the xerogel films, the range of ammonia concentration, that can be sensed, is extended. Fluorescence quenching for particle coatings occurred at concentrations between 1000–2500 ppm and for xerogel films between 10 000–40 000 ppm. All coatings show logarithmic behavior in NH_3 response. Coatings with only rhodamine labeled particles (PG SBA R 1, excited at 535 nm) and RBITC modified xerogel responded to NH_3 with a slight decrease in fluorescence emission intensity which can be explained by either the continuous deprotonation of the cationic species forming more zwitterionic species which results in decreased fluorescence emission intensity at 576 nm (Fig. 10c) or by reabsorption of rhodamine emission. This could also be another explanation for the decreasing intensity of rhodamine fluorescence emission for the PG SBA FR 2–4 coatings. Coatings with only FITC labeled particles (PG SBA F 1) responded logarithmically between 0–1000 ppm. A FITC modified xerogel responded linearly only from 200–1000 ppm.

Taking the calculated BET surface from Table 3, the amount of dye in a defined FRET sphere, with radius r = 5 nm, can be determined (Table 5). According to these results, less than one dye molecule is present in the required FRET distance of 10 nm. Since energy transfer is taking place, we suggest that the dye distribution is macroscopically homogenous as observed by CLSM. However, the dyes can be inhomogeneously distributed in a single hexagonal pore leading to irregular dye–dye distances and locally varying dye concentrations.

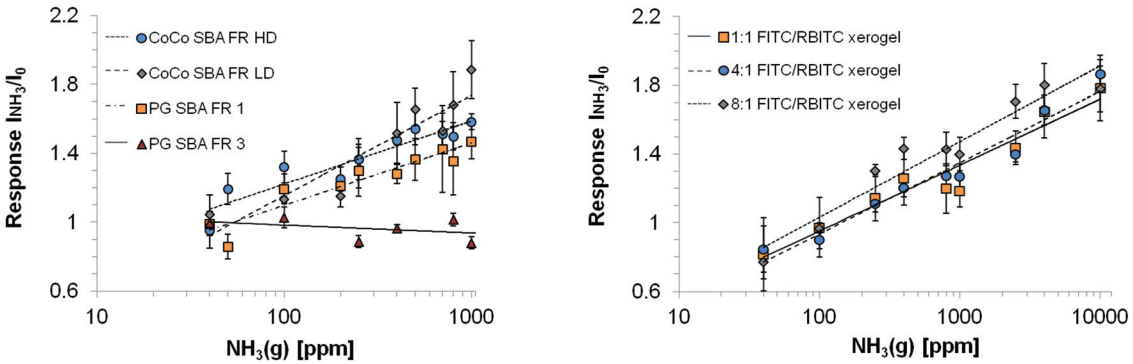

Fig. 9 Logarithmic dependency of rhodamine fluorescence emission intensity towards NH_3 for the investigated coatings. I_0 = fluorescence intensity of the reference (water), I_{NH_3} = fluorescence intensity in presence of ammonia. Excitation wavelength: 484 nm.

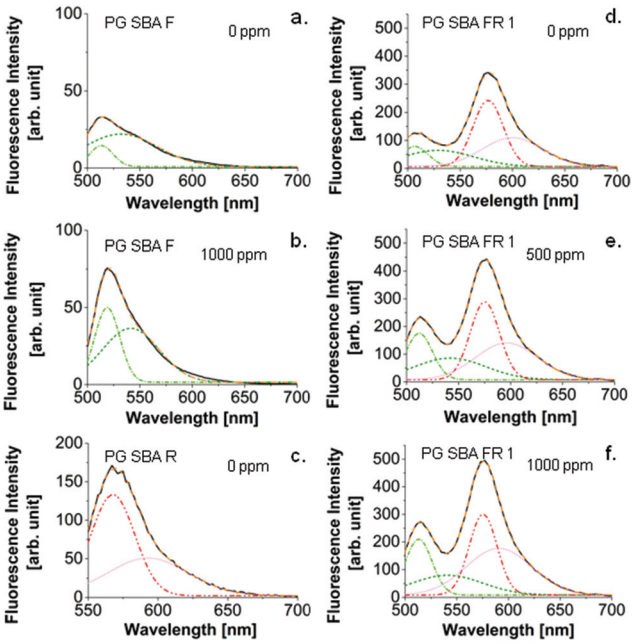

Fig. 10 Gaussian evaluation on the fluorescence spectra of PG SBA F, PG SBA R, and PG SBA FR 1. (a) PG SBA F exposed to 0 ppm NH_3; (b) PG SBA F exposed to 1000 ppm NH_3; (c) PG SBA R exposed to 0 ppm NH_3; (d) PG SBA FR 1 exposed to 0 ppm NH_3; (e) PG SBA FR 1 exposed to 500 ppm NH_3; (f) PG SBA 1 exposed to 1000 ppm NH_3. Gauss bands: light green: F dianion; dark green: F monoanion; red: R cation; pink: R zwitterion. Excitation wavelength: 484 nm.

Table 5 Amount of dye in a FRET sphere with a radius of 5 nm calculated from the BET surface

Sample	FITC	RBITC
CoCo SBA FR HD	1.23	0.46
CoCo SBA FR LD	0.08	0.04
PG SBA F	0.4	
PG SBA R		0.04
PG SBA FR 1	0.16	0.12
PG SBA FR 2	0.74	0.46
PG SBA FR 3	2.31	1.48
PG SBA FR 4	4.56	2.93

Gaussian evaluation. The emission wavelengths of the FRET dye pair are not completely separated, leading to an overlap between fluorescein and rhodamine emission. Exposure to NH_3 leads to an increase in the emission intensities of both dye molecules (fluorescein and rhodamine), because of the enhanced emission of deprotonated fluorescein on the one hand and the resulting increased FRET on the other hand. Therefore, it is difficult to estimate if the main gain in rhodamine intensity is caused by the enhanced energy transfer. Gaussian fitting to photoluminescence spectra is a common procedure for identifying the involved species which contribute to the final entire emission band.[55–57] To evaluate the contribution of the increasing fluorescein emission upon NH_3 exposure, to the increasing rhodamine emission, Gaussian fitting for the PG SBA FR 1 emission bands was performed. Only fluorescein and rhodamine labeled particles were fitted to find the peak wavelengths and fluorescence tail lengths of each species needed to account for the final spectra. As mentioned previously, the fluorescent species suggested for fluorescein are the monoanionic and dianionic forms and cationic and zwitterionic for rhodamine. Therefore, two Gaussians were fitted to each reference spectrum (Fig. 10a and c). Since intensity and peak wavelength is changed for fluorescein emission as a consequence of changed monoanionic/dianionic dye proportion upon NH_3 exposure, two Gaussians were fitted to a spectrum obtained upon exposure to 1000 ppm NH_3 (Fig. 10b). The values for peak wavelength and the full width at half maximum were set as initial values for the Gaussian fitting of the spectra obtained by fluorescein and rhodamine labeled PG particles (Fig. 10d–f).

Fig. 11 illustrates the trend in peak surface area received from the Gaussian evaluation on the fluorescence spectra of PG SBA FR 1 obtained upon exposure to 0, 250, 500, 1000 and 2000 ppm NH_3. With increasing NH_3 concentration, more fluorescein dianions are formed from further deprotonation of the fluorescein monoanions which is reflected in the increasing area of the corresponding Gaussian band located at *ca.* 512 nm. The maximum peak wavelength is red shifted with higher NH_3 concentrations from 507 to 514 nm. The fluorescein monoanion band increases from 0–500 ppm and starts to decrease when exposed to concentrations above 500 ppm. This observation suggests the presence of neutral species, which are deprotonated forming more monoanionic species. At the same time, deprotonation of mono- to dianonic species occurs. Above 500 ppm, every remaining neutral fluorescein species has been deprotonated and consequently no more monoanions can be formed resulting in deprotonation of only fluorescein monoanions and hence to the decrease in the peak surface area of the fluorescein monoanion. The maximum peak wavelengths show a significant red shift from 529 to 542 nm between 0 and 250 ppm NH_3. Subsequent increases in the NH_3 concentration do not lead to a further red shift.

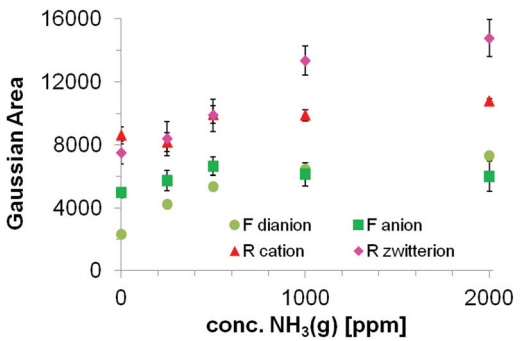

Fig. 11 Evolution in peak surface area for the different fluorescein and rhodamine dye species.

Both the rhodamine cation band located at 576 nm and the rhodamine zwitterion band located at *ca.* 590 nm, increase with increasing NH_3 concentration. Interestingly, the increase of the zwitterionic band occurs in a much higher extent (1.78 times) in comparison to the cationic band (1.15 times) and the maximum peak wavelength exhibits a blue shift of 10 nm. This indicates that the energy transfer from fluorescein to the zwitterionic form of rhodamine is preferred, assuming that no significant amount of rhodamine cation is converted to zwitterion due to the NH_3 exposure. The increase of both cationic and zwitterionic emissions of the rhodamine Gaussians is consistent with the energy transfer. Furthermore, only the fluorescein monoanion fluorescence emission can contribute to the rhodamine emission intensity because of its long emission tail. The fact that the Gaussian area of the fluorescein monoanionic species is decreasing with increasing NH_3 concentration supports the energy transfer model.

Gas sensor measurements. Images from optical microscopy and scanning electron microscopy showed homogenous distribution of the particles in the xerogel films (Fig. 12). CoCo SBA FR HD coatings tend to form larger particle agglomerations in comparison to the other particle coatings (Fig. 12a). Solvent casting of 20 μL of the reported sol solution on to a 1.5 × 1.5 × 0.1 cm^3 PMMA substrate resulted in smooth dry films with a thickness of 6 μm.[29] Coatings without particles display a smooth and even surface (Fig. 12d and f) whereas coatings with particles show an irregular surface with embedded SBA particles (Fig. 12a–c and e).

In order to investigate the dye accessibility of the coatings by the NH_3 gas, experiments were performed using the device shown schematically in Fig. 1. The gas flow was switched between a NH_3/N_2 gas mixture and pure N_2. When ammonia gas was introduced, it diffused into the xerogel film where deprotonation of the fluorescein dyes occurred, leading to the increase in rhodamine fluorescence emission. The dyes in the coatings were excited at 470 nm from the top of the gas sensor (Fig. 2). The PMMA substrate acted as a waveguide and the fluorescence intensity was thus monitored at the edge perpendicular to the irradiation. The long pass filter only allowed light of wavelengths from 550 nm to pass to the phototransistor. Thus, the change in fluorescence from 490 to 550 nm upon fluorescein deprotonation–protonation was not monitored. To reduce cross-sensitivity or cooling with humidified air, care was taken, that during switching the gases, the humidity did not exceed 4%. A measurement always started by purging the setup with gaseous N_2, which acted simultaneously as the reference gas and carrier gas. After 10 minutes, this valve was closed and the valve for purging with NH_3 gas was opened until the signal reached the maximum sensor response. The baseline was recovered by closing the NH_3-line and re-opening the N_2-line.

The top graph of Fig. 13 depicts the sensor response for the different coatings towards 1000 ppm NH_3. A similar response and change in rhodamine fluorescence intensity due to the energy transfer was obtained for the CoCo SBA FR HD and PG SBA FR 1 (Fig. 13, top, responses a and b) coatings in accordance with the above spectral investigations (Fig. 8). Because of the larger pore size and different morphology, the response time was slightly faster for the co-condensed material, due to

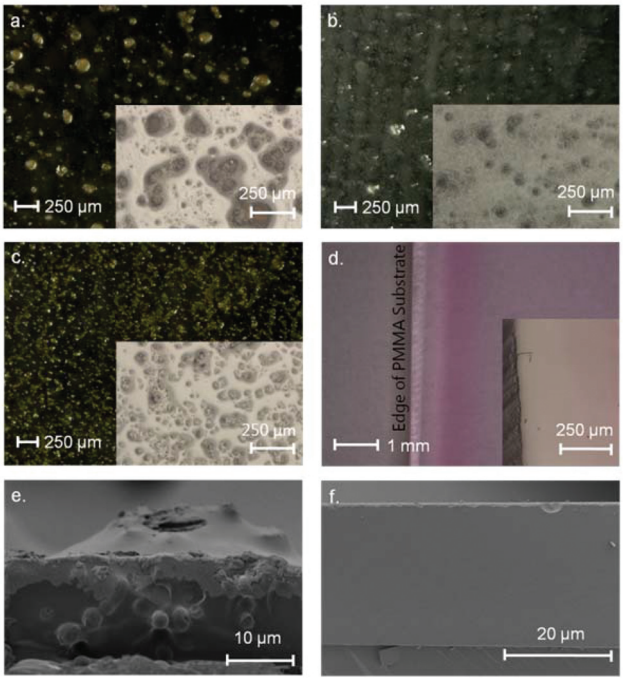

Fig. 12 Optical microscopy images of the investigated coatings. (a) CoCo SBA FR HD coating; (b) CoCo SBA FR LD coating; (c) PG SBA FR 1 coating; (d) 4 : 1 FITC/RBITC xerogel coating. SEM images. (e) Cut of PG SBA FR 1 coating; (f) Cut of 4 : 1 FITC/RBITC xerogel coating. The film thicknesses on the silicon wafers for the SEM images do not correspond to the thicknesses on the investigated PMMA substrates.

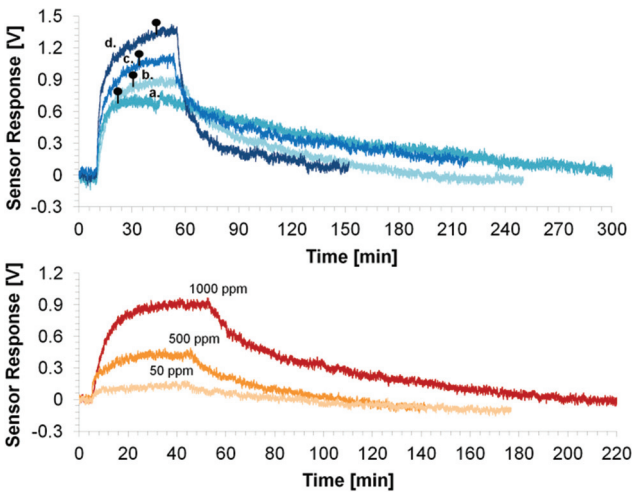

Fig. 13 Flow cell gas sensor response upon exposure to 1000 ppm gaseous NH_3. Top: (a) CoCo SBA FR HD coating; (b) PG SBA FR 1 coating; (c) unlabeled SBA in 4 : 1 FITC/RBITC xerogel coating; (d) 4 : 1 FITC/RBITC xerogel coating. The pins mark the time required to achieve 95% of the maximum sensor response. Bottom: response of PG SBA FR towards different NH_3 concentrations.

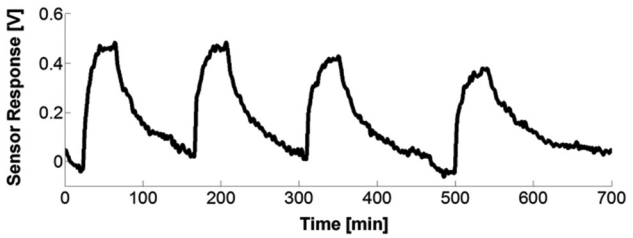

Fig. 14 Drift compensated cyclic response of the PG SBA FR 1 coating towards 500 ppm NH_3.

the faster diffusion of NH_3 into the coating. However, the co-condensed SBA had a much longer recovery time than the post-grafted SBA. It is reported that co-condensed mesoporous materials have a higher number of free hydroxyl groups on the surface due to the extraction of the template rather than calcination of the post-grafted materials.[58] Therefore, a possible reason for the lower recovery can be that the NH_3 gas is more strongly adsorbed by the co-condensed material by forming more hydrogen bonds with the free surface hydroxyl groups. In addition, the free silanol (SiOH) groups of the silica framework can be deprotonated by the basic NH_3 gas resulting in NH_4^+ and SiO^- leading to electrostatic NH_3 adsorption on the silica surface. Better responses were obtained for the 4 : 1 FITC/RBITC xerogel (Fig. 13, top, response d). Since the xerogel is very smooth, the NH_3 gas permeability is reduced, leading to the longer response time. The incorporation of unlabeled SBA into the xerogel coating did not lead to faster response and recovery times (Fig. 13, top, response c), as expected from the introduced porosity coming from the mesoporous particles. The exposure of the PG SBA FR 1 coating to different NH_3 gas concentrations led to different sensor responses (Fig. 13, bottom). The lowest detectable amount of ammonia with this setup was 10 ppm. Cyclic measurements with the PG SBA FR 1 coating (Fig. 14) demonstrate the reversibility of this coating by exhibiting the same loss and recovery in signal intensity in each cycle. The sensor response of the CoCo SBA FR HD coating was not reproducible since the long recovery time is subjected to thermal drift (electronic). This observation shows again the significance of the NH_3 adsorption on the silica surface. The signal response can be reproduced when warming the coating to 70 °C for 2 h.

4 Conclusion

The FRET activity of FITC and RBITC modified mesoporous SBAs has been studied by observing the change in RBITC fluorescence emission intensity when exposing the particles, immobilized into transparent xerogel coatings, to different NH_3 gas concentrations. Large dye loadings on the SBA lead to fluorescence quenching and hence to an inoperative FRET system. The impact of the different structural properties of co-condensed and post-grafted materials was investigated with a flow cell optical gas sensor setup built in-house. The response time was dependent on the structure of the immobilized SBA material, whereas the recovery time was strongly dependent on the surface properties of the material. The ability to adsorb the NH_3 molecules on the silica surface determines whether the particle coatings can be applied for reproducible and fully reversible sensor applications.

Acknowledgements

The authors gratefully acknowledge the financial support of Swiss National Science Foundation (SNF 140303). Special thanks go to our workshop team, L. Missaggia and M. Schmid for the sensor design and optimization of the electronics.

Notes and references

1 B. Lei, H. Zhang, S. Lu, Z. Zheng, W. Li and Y. Wang, *Adv. Funct. Mater.*, 2006, **16**, 1883–1891.
2 H. Zhang, Y. Sun, K. Ye, P. Zhang and Y. Wang, *J. Mater. Chem.*, 2005, **15**, 3181–3186.
3 X. Xu and H. Xiao, *J. Lumin.*, 2012, **132**, 2251–2258.
4 X. Wu, L. Song, B. Li and Y. Liu, *J. Lumin.*, 2010, **130**, 374–379; L.-L. Li, H. Sun, C.-J. Fang, J. Xu, J.-Y. Jin and C.-H. Yan, *J. Mater. Chem.*, 2007, **17**, 4492–4498.
5 R. Métivier, I. Leray, B. Lebeau and B. Valeur, *J. Mater. Chem.*, 2005, **15**, 2965–2973.
6 K. Kledzik, M. Orlowska, D. Patralska, M. Gwiazda, J. Jezierska, S. Pikus, R. Ostaszewski and A. M. Klonkowski, *Appl. Surf. Sci.*, 2007, **2**, 441–451.
7 L. Gao, Y. Wang, J. Wang, L. Huang, L. Shi, X. Fan, Z. Zou, T. Yu, M. Zhu and Z. Li, *Inorg. Chem.*, 2006, **45**, 6844–6850.
8 B. Xiao, J. Zhao, X. Liu, P. Wang and Q. Yang, *Microporous Mesoporous Mater.*, 2014, **199**, 1–6.
9 W. Jingxia, *J. Lumin.*, 2014, **151**, 41–46.
10 B. Wang, L. Zhang, B. Li, Y. Li, Y. Shi and T. Shi, *Sens. Actuators, B*, 2014, **190**, 93–100.
11 Z. Dong, X. Tian, Y. Chen, J. Hou and J. Ma, *RSC Adv.*, 2013, **3**, 2227–2233.
12 M. H. Lee, S. J. Lee, J. H. Jung, H. Lim and J. S. Kim, *Tetrahedron*, 2007, 12087–12092.
13 H. Zhang, P. Zhang, K. Ye, Y. Sun, S. Jiang, Y. Wang and W. Pang, *J. Lumin.*, 2006, **117**, 68–74.
14 F. Hoffmann, M. Cornelius, J. Morell and M. Fröba, *Angew. Chem., Int. Ed.*, 2006, **45**, 3216–3251.
15 T. Yokoi, H. Yoshitake and T. Tatsumi, *J. Mater. Chem.*, 2004, **14**, 951–957.
16 H. H. Lim and A. Stein, *Chem. Mater.*, 1999, **11**, 3285–3295.
17 D. Brühwiler, *Nanoscale*, 2010, **2**, 887–892.
18 N. Gartmann and D. Brühwiler, *Angew. Chem., Int. Ed.*, 2009, **48**, 6354–6356.
19 N. Gartmann, C. Schütze, H. Ritter and D. Brühwiler, *J. Phys. Chem. Lett.*, 2010, **1**, 379–382.

20 S. Huh, J. W. Wiench, B. G. Trewyn, S. Song, M. Pruski and V. S.-Y. Lin, *Chem. Commun.*, 2003, 2364–2365.
21 K. Möller, J. Kobler and T. Bein, *J. Mater. Chem.*, 2006, **17**, 624–631.
22 F. O. M. Gaslain, C. Delacôte, A. Walcarius and B. Lebeau, *J. Sol-Gel Sci. Technol.*, 2009, **49**, 112–124.
23 J. M. Rosenholm and M. Lindén, *Chem. Mater.*, 2007, **19**, 5023–5034.
24 J. R. Lakowicz, in *Principles of Fluorescence Spectroscopy*, Springer, New York, 3rd edn, 2010, pp. 445–453.
25 Y. Ma, L. Qi, J. Ma, Y. Wu, O. Liu and H. Cheng, *Colloids Surf., A*, 2003, **229**, 1–8.
26 A. Katiyar and N. G. Pinto, *Small*, 2006, **2**, 644–648.
27 L. Wang, T. Qi, Y. Zhang and J. Chu, *Microporous Mesoporous Mater.*, 2006, **91**, 156–160.
28 J. Lei, L. Wang and J. Zhang, *Chem. Commun.*, 2010, **46**, 8445–8447.
29 S. Widmer, M. Dorrestijn, A. Camerlo, S. K. Urek, A. Lobnik, C. E. Housecroft, E. C. Constable and L. J. Scherer, *Analyst*, 2014, **139**, 4335–4342.
30 E. P. Perman, *J. Chem. Soc.*, 1901, **79**, 718–725.
31 E. P. Perman, *J. Chem. Soc.*, 1903, **83**, 1168–1184.
32 S. Brunauer, P. H. Emmett and E. Teller, *J. Am. Chem. Soc.*, 1938, **60**, 309–319.
33 J. Landers, G. Y. Gor and A. V. Neimark, *Colloids Surf., A*, 2013, **437**, 3–32.
34 M. Kruk, M. Jaroniec, R. Ryoo and J. M. Kim, *Microporous Mater.*, 1997, **12**, 93–106.
35 P. I. Ravikovitch and A. V. Neimark, *J. Phys. Chem. B*, 2001, **105**, 6817–6823.
36 Q. Huo, D. I. Margolese, U. CIesla, D. G. Demuth, P. Feng, T. E. Gier, P. Sieger, A. Firouzi and B. F. Chmelka, *Chem. Mater.*, 1994, **6**, 1176–1191.
37 N. Gartmann and D. Brühwiler, *Materials*, 2011, **4**, 1096–1103.
38 F. López Arbeloa, P. Ruiz Ojeda and I. López Arbeloa, *J. Lumin.*, 1989, **44**, 105–112.
39 H. Ritter and D. Brühwiler, *J. Phys. Chem. C*, 2009, **113**, 10667–10674.
40 L. Peng, X. Yang, L. Yuan, L. Wang, E. Zhao, F. Tian and Y. Liu, *Opt. Commun.*, 2011, **284**, 4810–4814.
41 A. Persad, K.-F. Chow, W. Wang, E. Wang, A. Okafor, N. Jespersen, J. Mann and A. Bocarsly, *Sens. Actuators, B*, 2008, **129**, 359–363.
42 Y. Takagai, Y. Nojiri, T. Takase, W. L. Hinze, M. Butsugan and S. Igarashi, *Analyst*, 2010, **135**, 1417–1425.
43 T. Abel, B. Ungerbock, I. Klimant and T. Mayr, *Chem. Cent. J.*, 2012, **6**, 124.
44 C. Preininger, M. Ludwig and G. J. Mohr, *J. Fluoresc.*, 1998, **8**, 199–205.
45 Q. Chang, J. Sipior, J. R. Lokowicz and G. Rao, *Anal. Biochem.*, 1995, **232**, 92–97.
46 K. Waich, S. Borisov, T. Mayr and I. Klimant, *Sens. Actuators, B*, 2009, **139**, 132–138.
47 J. Lei, L. Wang and J. Zhang, *Chem. Commun.*, 2010, **46**, 8445–8447.
48 R. Sjöback, J. Nygren and M. Kubista, *Spectrochim. Acta, Part A*, 1995, **51**, L7–L21.
49 M. M. Martin and L. Lindqvist, *J. Lumin.*, 1975, **10**, 381–390.
50 H. Leonhardt, L. Gordon and R. Livingston, *J. Phys. Chem.*, 1971, **75**, 245–249.
51 R. W. Ramette and E. B. Sandell, *J. Am. Chem. Soc.*, 1956, **78**, 4872–4878.
52 S. Woislawski, *J. Am. Chem. Soc.*, 1953, **75**, 5201–5203.
53 S.-L. Hii, S.-Y. Yong and C.-L. Wong, *J. Appl. Phycol.*, 2009, **21**, 625–631.
54 Y. A. Gomaa, M. J. Garland, F. McInnes, R. F. Donnelly, L. K. El-Khordagui and C. Wilson, *Int. J. Pharm.*, 2012, **438**, 140–149.
55 A. J. G. Otuka, V. Tribuzi, D. S. Corrêa and C. R. Mendonça, *Opt. Mater. Express*, 2012, **2**, 1803–1808.
56 L. Zhang, Z. Fu, Z. Wu, Y. Wang, X. Fu and T. Cui, *Mater. Res. Bull.*, 2014, **56**, 65–70.
57 Q. Wang, Z. Ci, G. Zhu, M. Que, S. Xin, Y. Wen and Y. Wang, *J. Solid State Sci. Technol.*, 2012, **1**, R92–R97.
58 F. Kleitz, W. Schmidt and F. Schüth, *Microporous Mesoporous Mater.*, 2003, **65**, 1–29.